The Astrophysical Journal, 958:40 (6pp), 2023 November 20 https://doi.org/10.3847/1538-4357/ad0548

Updated Reference Wavelengths for Si VII and Mg VII Lines in the 272–281 Å Range

Peter R. Young[1,2]
[1] NASA Goddard Space Flight Center, Greenbelt, MD 20771, USA
[2] Northumbria University, Newcastle upon Tyne, NE1 8ST, UK
Received 2023 March 7; revised 2023 October 15; accepted 2023 October 18; published 2023 November 10

Abstract

New reference wavelengths for atomic transitions of Mg VII and Si VII in the 272–281 Å wavelength range are derived using measurements from the Extreme-ultraviolet Imaging Spectrometer (EIS) on board the Hinode spacecraft. Mg VII and Si VII are important ions for measuring plasma properties in the solar transition region at around 0.6 MK. The six Si VII wavelengths are 13–21 mÅ and 7–11 mÅ longer than the values in the NIST Atomic Spectra Database (ASD) and the compilations of B. Edlén, respectively. The four Mg VII wavelengths are shorter than the values in the ASD by 8–12 mÅ but show reasonable agreement with the Edlén values. The new wavelengths will lead to more accurate Doppler shift measurements from the EIS instrument and will be valuable for spectral disambiguation modeling for the upcoming Multi-Slit Solar Explorer mission.

Unified Astronomy Thesaurus concepts: Ultraviolet spectroscopy (2284); Solar atmosphere (1477); Solar transition region (1532); Atomic data (2216)

1. Introduction

Mg VII and Si VII are formed at a temperature of 0.6 MK in electron-ionized plasmas and give rise to 10 emission lines in the 272–281 Å wavelength range. These lines have been observed by the Extreme-ultraviolet Imaging Spectrometer (EIS; Culhane et al. 2007) on board the Hinode spacecraft since 2006, and they provide valuable diagnostics of the upper transition region. For example, the Mg VII λ280.73/λ278.39 ratio is an excellent diagnostic of the electron number density (Young et al. 2007) that has been used to obtain the density variation along coronal loops (Tripathi et al. 2009; Young et al. 2012). The Si VII λ275.37 line is often used for Doppler velocity measurements (Ugarte-Urra & Warren 2011) and is an important "anchor line" for accounting for the time-variable wavelength offset between the short- and long-wavelength channels of EIS (Young et al. 2012).

Landi & Young (2009) highlighted that there are significant discrepancies for the Mg VII and Si VII reference wavelengths between the tabulations in the National Institute for Standards and Technology (NIST) Atomic Spectra Database[3] (ASD) and those provided by B. Edlén (Edlén 1983, 1985). The present work provides updated reference wavelengths for these lines based on measurements obtained from the EIS spectra.

All data and software used in this article are publicly available, and Section 2 gives the sources. Section 3 presents the Mg VII and Si VII lines studied here, and Section 4 gives some properties of the cool coronal loops that are analyzed. Section 5 describes the EIS instrument and explains the choice of data sets, and Section 6 details the data analysis procedure used to derive the new reference wavelengths. Section 7 gives new experimental energies obtained from the wavelengths, and a summary of the article is given in Section 8.

[3] https://www.nist.gov/pml/atomic-spectra-database

2. Data and Software Availability

Data from the Hinode/EIS instrument are analyzed in this article, and the level-0 (uncalibrated) data are publicly available from the Virtual Solar Observatory[4] and the Hinode Science Data Centre Europe.[5] The EIS data are calibrated using IDL software available in the public repository *Solarsoft* (Freeland & Handy 1998, 2012), which also contains routines for extracting spectra and fitting Gaussians as described in the following text. Derived data products from the present analysis are made available through Zenodo at doi:10.5281/zenodo.8368508 and include Gaussian line fit parameters from which the emission-line wavelengths are derived. The data files used as input to the LOPT code (Section 7) are available through a separate Zenodo entry at doi:10.5281/zenodo.10001618. IDL routines for generating the figures in this article are available through a GitHub repository[6] in the folder 2023_mg7_si7.

3. The Mg VII and Si VII Lines

Mg VII belongs to the carbon isoelectronic sequence, and the EIS wavelength ranges contain four emission lines corresponding to the $2s^2 2p^2\ ^3P_J$–$2s2p^3\ ^3S_1$ ($J = 0, 1, 2$) and $2s^2 2p^2\ ^1D_2$–$2s2p^3\ ^1P_1$ transitions with wavelengths between 276 and 281 Å. Of the ^3P_J–$^3S_1$ transitions, only the weakest line at 276.14 Å is unblended. The strongest line at 278.39 Å is blended with Si VII λ278.46 but can be resolved through a two-Gaussian fit, for example. The $^3P_1$–$^3S_1$ transition at 276.99 Å is blended with two Si VIII lines, and it is not possible to resolve this feature without using information from one of the other Mg VII lines (Landi & Young 2009). The $^1D_2$–$^1P_1$ transition at 280.73 Å is unblended and makes an excellent density diagnostic with either of the λ276.14 or λ278.39 lines (Young et al. 2007).

[4] https://sdac.virtualsolar.org/cgi/search
[5] http://sdc.uio.no/sdc/
[6] https://github.com/pryoung/papers

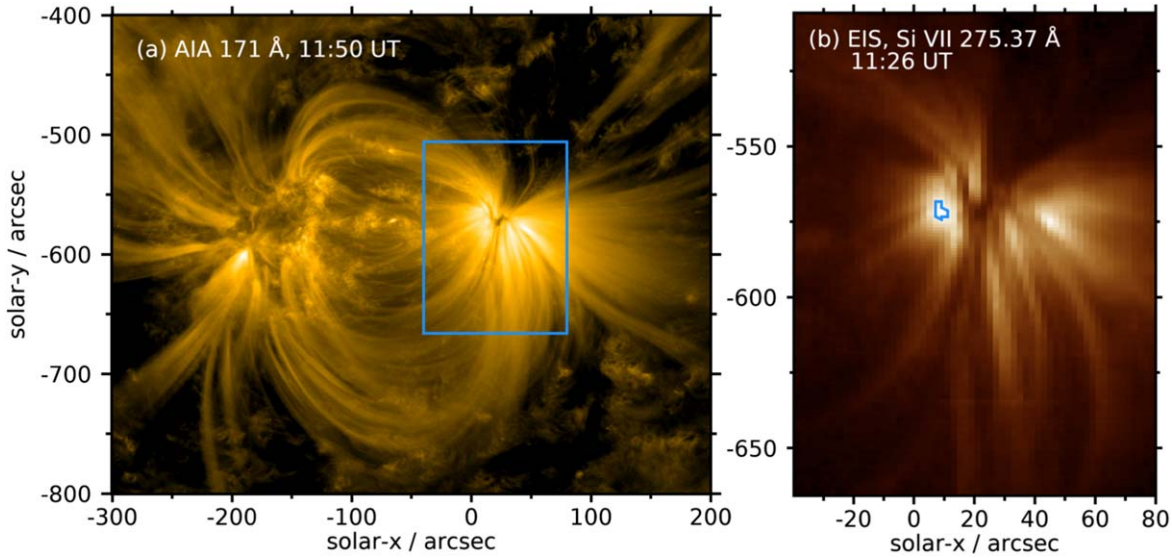

Figure 1. (a) An AIA 171 Å image (logarithmic scaling) showing an active region from 2010 September 22. The blue box shows the region rastered by EIS. (b) An EIS image (linear scaling) formed from the Si VII λ275.37 line observed in the raster beginning 11:26 UT. The blue contour shows the spatial region averaged to yield the spectrum from which wavelength measurements were made in the present work. Three adjacent data columns between $x = 66''$ and $x = 72''$ are missing in the EIS data and have been interpolated for display purposes.

Si VII is a member of the oxygen isoelectronic sequence, and the six members of the $2s^2 2p^4\ ^3P_J$–$2s2p^5\ ^3P_{J'}$ ($J = 0,\ 1,\ 2; J' = 0,\ 1,\ 2$) multiplet are found between 272 and 279 Å, close to the Mg VII lines discussed above. The 0–1 transition occurs at 276.86 Å and is blended with two Si VIII lines. As for the Mg VII line mentioned above, it is not possible to resolve this blend without using information from one of the other Si VII lines, and so it is not useful for the present analysis. The 1–2 transition is partially blended with a stronger Mg VII line, as discussed above. The 1–0 transition at 274.19 Å is blended with Fe XIV λ274.20 but is important as the only line that determines the $2s2p^5\ ^3P_0$ energy. The multiplet's lines show density sensitivity relative to each other, and they are most sensitive around 2×10^8 cm^{-3}, but this is too low for structures in the low solar atmosphere.

4. Cool Loops

Solar active regions often have loops at their peripheries that are rooted in decaying plage or sunspots. These loops are bright in Fe IX and Fe X, formed around 0.8–1.0 MK, and they came to prominence when the Transition Region and Coronal Explorer (Handy et al. 1999) began taking high-resolution images in a filter centered at 173 Å. These images were dominated by emission from Fe IX λ171.07 and Fe X λ174.53. The loops are also observed in images from the Atmospheric Imaging Assembly (AIA; Lemen et al. 2012) on board the Solar Dynamics Observatory, which has a channel centered at 171 Å that is dominated by Fe IX. Figure 1(a) shows an AIA 171 Å image for an active region studied in the present work, observed on 2010 September 22. As the loops are cooler than the shorter loops in the active region center, they are often referred to as "cool" loops.

For ions formed at lower temperatures, the emission is increasingly concentrated at the footpoints of the cool loops (Figure 1(b)) and has been studied with the Coronal Diagnostic Spectrometer (Harrison et al. 1995) on board the Solar and Heliospheric Observatory, as well as Hinode/EIS. In particular, the emission lines of ions of magnesium, silicon, and iron are strongly enhanced in the temperature range 0.4–0.8 MK (see Figure 4 of Young et al. 2007). Spectral atlases and detailed plasma diagnostics of cool loop footpoints have been presented by Landi & Young (2009), Young & Landi (2009), and Del Zanna (2009). The high signal-to-noise ratios of cool loop footpoint spectra make them ideal for obtaining reference wavelengths for lines in the 0.4–0.8 MK temperature range, and they have been used recently for reassessments of energy levels of Fe VII (Young et al. 2021; Kramida et al. 2022) and Fe IX (Ryabtsev et al. 2022).

Table 1
Identifiers for the EIS Data Files Used in the Present Analysis

File ID	
20070105_2152	20070106_1555
20070115_2217	20070123_1540
20070221_0015	20070221_0112
20070524_1229	20100801_2339
20100809_0341	20100922_1126
20110122_1512	20160520_0050
20170713_1251	

5. The EIS Instruments and Data Sets

EIS is an imaging slit spectrometer that obtains spectra in the 170–212 Å and 246–292 Å wavelength ranges at a resolution of 3000–4000. Only data from the long-wavelength channel are used in the present work. There is a choice of four slits with different widths, and only data from the narrow 1″ and 2″ slits are used here. The instrument spatial resolution is 3″–4″ (Young & Ugarte-Urra 2022), and the detector pixels correspond to an angular size of 1″.

Thirteen EIS data sets were used for the present analysis. All are spatial rasters that yield the entire spectral range of the EIS instrument, and all are active region data sets in which cool loop footpoints are prominent. The file IDs for the data sets are given in Table 1. The first eight characters give the date in year-month-day format, and the last four characters give the start

time of the observation in hours and minutes, e.g., "2152" corresponds to 21:52 UT. The data set 20070105_2152 was previously studied by Del Zanna (2009), and the data set 20070221_0112 was previously studied by Landi & Young (2009) and Young & Landi (2009), although the spectra derived here were obtained from different spatial regions.

The data sets were selected either from those already known by the author or by browsing the EIS mapper[7] (Young 2022a) products that show the locations of EIS rasters on full-disk solar EUV images. For the latter, rasters were sought that included bright loop footpoints as seen in the AIA 171 Å channel. Inspection of selected data sets was performed to avoid footpoints for which there was significant hot (1–3 MK) emission in the line of sight in order to minimize blending. There was a particular focus on data sets from 2007 when EIS was in a near-pristine condition. In particular, the number of warm pixels on the EIS detectors was low, and the sensitivity of the long-wavelength channel was high.

The Si VII λ274.19 line is blended with Fe XIV λ274.20 (formed at 2 MK). Potentially this can be resolved by considering data from an on-disk coronal hole, where Fe XIV is expected to be negligible owing to the low temperature in coronal holes (e.g., Del Zanna & Bromage 1999). However, instrument scattered light (Wendeln & Landi 2018; Young & Viall 2022) results in a baseline intensity component to hot emission lines within coronal holes, and it was determined that the cool loop footpoints are preferable as locations where Si VII dominates Fe XIV at 274.2 Å.

The spectra from each data set were prepared as follows. An image from the raster was formed in the Si VII λ275.37 line, and a location was chosen where the line emission was strong. A number of spatial pixels around this location were averaged to yield a single spectrum (e.g., Figure 1(b)). The number of pixels selected varied from 10 to 32. The averaging was done using the IDL routine eis_mask_spectrum (Young 2022b), and the output spectra are available at Zenodo doi:10.5281/zenodo.8368508.

6. Data Analysis

Deriving absolute reference wavelengths for EUV emission lines using solar spectra requires some assumptions, as plasma motions can lead to Doppler shifts of tens of mÅ. In addition, EUV instruments cannot be flown with wavelength calibration lamps, and so the absolute wavelength scale is not known. A common practice is to assume that measurements made above the solar limb in a quiet part of the solar atmosphere represent plasma with zero Doppler shift. This is because the solar magnetic field is approximately parallel to the Sun's radius and plasma is constrained to move along the magnetic field direction in the low corona. Thus, motions will be mostly perpendicular to the line of sight at the limb and will not give rise to Doppler shifts. In addition, the long plasma column depth above the limb serves to smooth out any small spatial scale plasma motions.

The quiet Sun off-limb spectrum thus gives a zero Doppler shift spectrum, but there remains the problem of the unknown absolute wavelength calibration. For this, the Behring et al. (1976) rocket spectrum is used. This high-resolution, full-disk solar spectrum was calibrated using known wavelengths of various cool emission lines in the solar spectrum. By adjusting lines in the EIS spectrum to be consistent with those in the Behring et al. (1976) spectrum, the absolute wavelength scale can be set.

This method potentially allows all of the Si VII and Mg VII lines in the EIS spectrum to be measured. However, these lines are weak in off-limb regions, which typically have temperatures around 1.0–1.5 MK (Warren & Brooks 2009), and only the Si VII λ275.37 line can be reliably measured. The EIS off-limb measurements of Warren et al. (2011) are used, which include the Si VII line as well as the Fe XIV λ274.20 and Fe XV λ284.16 lines. The latter are in the Behring et al. (1976) line list with an accuracy of 4 mÅ. (The Si VII line is also present, but with a low accuracy of 10 mÅ.) An offset to the Warren et al. (2011) wavelengths is therefore obtained by adjusting the Fe XIV and Fe XV lines to best match the Behring et al. (1976) wavelengths. This offset then gives a Si VII reference wavelength of 275.368 Å with an uncertainty of 4 mÅ, which is the uncertainty of the Behring et al. (1976) coronal line measurements.

With the Si VII λ275.37 reference wavelength obtained, the high signal-to-noise ratio cool loop footpoint spectra are then used to derive wavelength offsets for the remaining Si VII and Mg VII lines relative to this line. Since CHIANTI predicts these two ions to be formed at the same temperature, they are expected to display the same Doppler shifts, and so there should be no relative offset between the two ions. This is confirmed here by both Doppler shift and intensity measurements (see below).

The wavelength offsets were obtained as follows. For each of the 13 cool loop spectra, emission lines were manually fit with Gaussians using the spec_gauss_eis routine (Young 2022b). Of the 10 Mg VII and Si VII lines, two are not analyzed here, as they are blended (Section 3). Four of the lines are isolated and could be fit with single Gaussians. The Si VII λ272.66 line has an unknown, weak line on the short-wavelength side that was masked out from the fit (Figure 2(a)). The blend at 274.2 Å containing a Si VII line and an Fe XIV line was fit as a single Gaussian; however, there is an unknown, weak line on the short-wavelength side apparent in some spectra (Figure 2(b)) that was fit with a second Gaussian. As noted earlier, the Mg VII λ278.39 and Si VII λ278.46 lines are partially blended and were fit together using two Gaussians forced to have the same width (Figure 2(c)). The latter is justified, as the two ions are emitted at the same temperature, and hence their thermal widths will be very similar.

In addition to the above lines, a two-Gaussian fit was applied to the blend of Mg VI λ270.39 and Fe XIV λ270.52. The intensity of the latter is used to estimate the strength of Fe XIV λ274.20, which blends with one of the Si VII lines. The $\lambda 274.20/\lambda 270.52$ ratio is weakly density sensitive with a value $\leqslant 2$ for densities above 10^9 cm^{-3}, which are typical of the active region corona. Therefore, the 270.52 Å intensity is multiplied by two to give an upper limit intensity for the Fe XIV λ274.20 line.

For each of the Si VII and Mg VII lines except Si VII λ274.19, the measured wavelengths were used to derive the wavelength separations relative to Si VII λ275.37. The average separation, $\Delta\lambda$, for each line is shown in Table 2. The uncertainty is obtained from the standard deviation of the 13 measured values.

For Si VII λ274.19 there is a risk that the the Fe XIV blend skews the wavelength measurement. To minimize this, the

[7] https://eismapper.pyoung.org

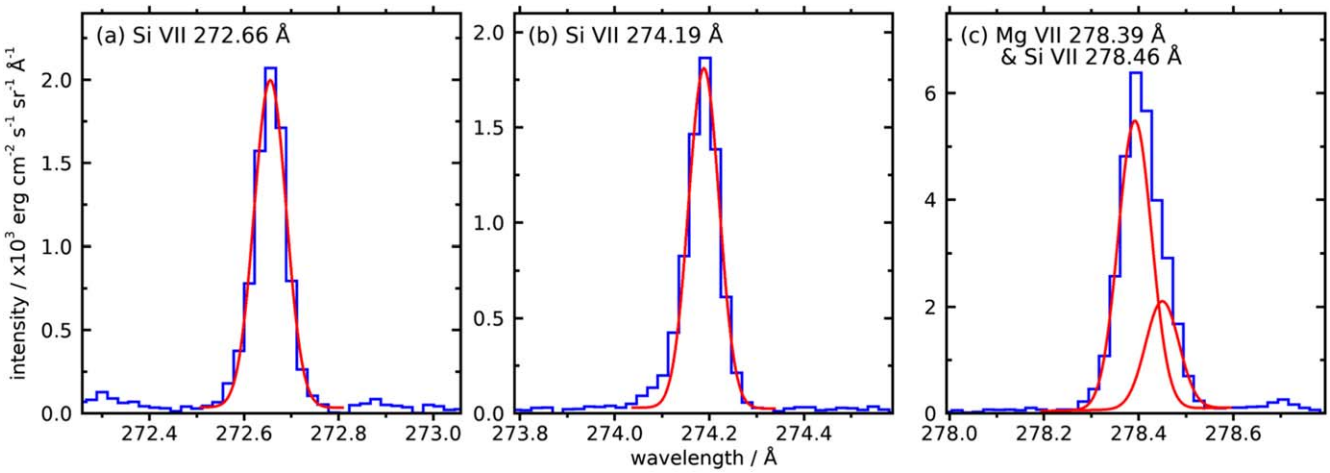

Figure 2. Line profiles from the 20070221_0115 data set. The spectra are shown in blue, and Gaussian fits to the lines are shown in red. Panel (c) shows the two-Gaussian fit for this blended feature.

Table 2
Si VII and Mg VII Transitions and Wavelengths

Ion	Configurations	Terms	$\Delta\lambda$[a]/Å	Wavelengths (Å)			
				Measured[a]	Ritz[a]	ASD	Edlén
Si VII	$2s^22p^4$–$2s2p^5$	$^3P_2$–$^3P_1$	−2.7105(9)	272.658 (4)	272.658 (3)	272.639	272.647
		$^3P_1$–$^3P_0$	−1.1804(13)	274.188 (4)	274.188 (4)	274.175	274.180
		$^3P_2$–$^3P_2$	0.0000	275.368 (4)	275.368 (3)	275.353	275.361
		$^3P_1$–$^3P_1$	+0.3158(8)	275.684 (4)	275.685 (3)	275.667	275.675
		$^3P_0$–$^3P_1$	…	…	276.860 (3)	276.839	276.850
		$^3P_1$–$^3P_2$	+3.0877(27)	278.456 (5)	278.456 (3)	278.443	278.449
Mg VII	$2s^22p^2$–$2s2p^3$	$^3P_0$–$^3S_1$	+0.7739(10)	276.142 (4)	276.142 (3)	276.154	276.138
		$^3P_1$–$^3S_1$	…	…	276.993 (3)	277.001	276.993
		$^3P_2$–$^3S_1$	+3.0261(18)	278.394 (4)	278.394 (3)	278.402	278.393
		$^1D_2$–$^1P_1$	+5.3613(14)	280.729 (4)	280.729 (4)	280.737	280.722

Note. The Ritz wavelengths are the recommended values.
[a] The number in parentheses gives the uncertainty on the last digit(s).

intensity ratio of the measured line relative to Si VII λ275.37 is computed, and only data sets with ratios $\leqslant$0.4 are retained. The theoretical Si VII λ274.19/λ275.37 ratio from CHIANTI (Dere et al. 2023) ranges from 0.21 to 0.26 over the density range from 10^9 to 10^{10} cm^{-3} expected for the cool loop footpoints; hence, the requirement is to ensure a dominant Si VII contribution. In addition, the Fe XIV λ270.52 intensity is multiplied by two and then divided by the measured λ274.19 intensity. Only data sets for which this ratio is $<$0.5 are retained. Seven data sets satisfy these two criteria, and the wavelength differences are averaged to yield the $\Delta\lambda$ value in Table 2.

The $\Delta\lambda$ standard deviations for the two unblended Mg VII lines are small, translating to $<$1.5 km s^{-1} in Doppler motions. This confirms the assumption that Mg VII is formed very close in temperature to Si VII, and thus they exhibit very similar Doppler motions in solar plasmas. This is backed up by the intensity ratio of Mg VII λ276.14 to Si VII λ275.37, which shows little variation between the data sets. It lies between 0.17 and 0.21 (mean value of 0.186) for 12 of the data sets, with the 20070123 data set anomalous in having a ratio of 0.26. Although not directly relevant to the present article, it is to be noted that the CHIANTI atomic models combined with the Asplund et al. (2021) solar photospheric abundances predict a λ276.14/λ275.37 ratio of 0.119. The higher ratios found in the cool loop footpoints may be due to an enhanced magnesium abundance (by around 50%).

7. Derivation of Level Energies

The wavelength measurements presented here allow the energies of the five upper levels of the Mg VII and Si VII transitions to be determined when combined with independent measurements of the ground configuration level energies. The wavelengths are input to the publicly available LOPT code (Kramida 2011) that was developed at NIST in order to derive an optimized set of level energies from a set of wavelength measurements. Where there are multiple measured wavelengths that constrain a level's energy, the code finds the optimum energy value given the measurement uncertainties. For the present work, we consider only the measured wavelengths from the EIS data (given in the fifth column of Table 2) together with the forbidden transition data discussed below. A comprehensive study of all energy levels that utilizes additional laboratory and space measurements will be performed in a follow-up work.

Table 3 lists the measurements of the forbidden transitions within the ground configurations of Mg VII and Si VII that are used here. They are obtained from infrared (IR) and far-UV spectra of the Sun and astrophysical nebula sources. Kelly & Lacy (1995) measured the Mg VII $^3P_0$–$^3P_1$ transition, but the

Table 3
Forbidden Line Wavelength Measurements

Ion	Configuration	Transition	Wavelength	Units	Reference
Si VII	$2s^22p^4$	$^3P_2$–$^3P_1$	4026.84 ± 0.20	cm^{-1}	Reconditi & Oliva (1993)
		$^3P_1$–$^3P_0$	1540.29 ± 0.25	cm^{-1}	Feuchtgruber et al. (1997)
Mg VII	$2s^22p^2$	$^3P_0$–$^3P_1$	1112.2 ± 0.2	cm^{-1}	See main text.
		$^3P_1$–$^3P_2$	1817.10 ± 0.41	cm^{-1}	Feuchtgruber et al. (1997)
		$^3P_2$–$^1D_2$	2629.674 ± 0.221	Å	Young et al. (2006)

identification was disputed by Feuchtgruber et al. (1997), who suggested that the line was instead due to Ar III. Beintema & Pottasch (1999) provided a line list for NGC 6302 and confirmed this suggestion. Pottasch & Beintema (1999) derived a temperature and density for NGC 6302 using emission-line diagnostics and the Beintema & Pottasch (1999) line list. From the CHIANTI 10.1 Mg VII model (Dere et al. 2023), the flux ratio of the 9.0 μm line to the 5.5 μm line should be 1.16, which then implies that Mg VII is responsible for 94% of the 9.0 μm flux reported by Beintema & Pottasch (1999). However, Pottasch & Beintema (1999) assumed that the line was dominated by Ar III, which is supported by additional Ar III lines, as well as the large fluxes of Ar II and Ar V lines. Inspection of the publicly available Infrared Space Observatory spectra of NGC 6302 does not show an obvious alternative identification for the Mg VII line, but future observations of NGC 6302 with the Mid Infrared Instrument on board the James Webb Space Telescope may resolve this issue.

Assuming that the Mg VII 9.0 μm line is blended with Ar III, an energy of 1112.2 ± 0.2 cm^{-1} can be assigned to the $^3P_0$–$^3P_1$ transition, corresponding to a wavelength of 8.991 μm. The uncertainty comes from assuming that the Mg VII line is found somewhere within the Ar III profile, which is about 0.4 cm^{-1} wide at the base (Figure 2 of Kelly & Lacy 1995).

The separations of the EUV lines are found to be consistent with the infrared wavelengths. For example, the Si VII $\lambda\lambda$272.658 and 275.685 line separation is measured to be 3.0263 ± 0.0011 Å. This implies a separation of 4026.1 ± 1.4 cm^{-1} for the ground $^3P_{2,1}$ levels, consistent with the infrared measurement (Table 3). The Mg VII $\lambda\lambda$276.142 and 278.394 lines imply a separation of 2929.6 ± 1.7 cm^{-1} for the ground $^3P_{0,2}$ levels. Combining the two IR lines gives a separation of 2929.30 ± 0.46 cm^{-1}, consistent with the EIS measurements.

Table 4 gives the final energies and uncertainties obtained from LOPT for Mg VII and Si VII. They are compared with the values from the NIST ASD, which derive from the compilations of Martin & Zalubas (1980) and Martin & Zalubas (1983) for magnesium and silicon, respectively. B. Edlén performed a number of analyses of energy levels along isoelectronic sequences, and his values for Mg VII and Si VII are given in the fourth column of Table 4. These values were published in Edlén (1983) and Edlén (1985) for Si VII and Mg VII, respectively. The ASD values show differences of up to 26 cm^{-1} compared to the present energies for the levels in the excited configurations. In all cases, the Edlén energies are closer to those found here.

The Ritz wavelengths (derived from the optimized level energies) are given in the sixth column of Table 2, and these are the recommended wavelengths to be used when deriving Doppler shifts from EIS. They can be compared with the ASD and Edlén wavelengths given in the seventh and eighth columns of Table 2, respectively. The ASD wavelengths for

Table 4
Comparison of Si VII and Mg VII Energies with Previous Values

Level	Energy (cm^{-1})		
	Present[a]	ASD	Edlén
Si VII (ground: $^3P_2$)			
$2s^22p^4\ ^3P_1$	4026.8 (2)	4030	4028
$^3P_0$	5567.1 (2)	5565	5568
$2s^22p^5\ ^3P_2$	363,150 (4)	363,170	363,160
$^3P_1$	366,760 (4)	366,786	366,774
$^3P_0$	368,740 (5)	368,761	368,752
Mg VII (ground: $^3P_0$)			
$2s^22p^2\ ^3P_1$	1112.2 (2)	1107	1118
$^3P_2$	2929.3 (5)	2929	2933
$^1D_2$	40,956.8 (32)	40,948	40,957
$2s2p^3\ ^3S_1$	362,132 (4)	362,117	362,138
$^1P_1$	397,172 (6)	397,153	397,181

Note.
[a] The uncertainty on the last digit(s) of the energy is given in parentheses.

Si VII are systematically smaller by 13 to 21 mÅ, while they are systematically larger for Mg VII by 8−12 mÅ. The Edlén wavelengths for Si VII are also systematically smaller than the present values by 7−11 mÅ, but the Mg VII wavelengths are in good agreement, except for the λ280.73 line, which is lower by 7 mÅ in the Edlén work.

8. Summary and Discussion

The sixth column of Table 2 gives new reference wavelengths for the Mg VII and Si VII emission lines observed by Hinode/EIS between 272 and 281 Å. These values are recommended to EIS users for deriving Doppler shift velocities for these two ions. The new wavelengths are combined with the literature values for the ions' forbidden lines to yield new experimental energies for the transitions' levels (second column of Table 4).

The new wavelengths should be valuable for the upcoming NASA Multi-slit Solar Explorer (De Pontieu et al. 2020) mission, which will perform spectroscopy in three EUV channels. One of these is centered at 284 Å and will include the Mg VII and Si VII lines discussed in this article. As the instrument uses multiple parallel slits, the resulting spectra will overlap on the detector, requiring disambiguation using synthetic spectra (Cheung et al. 2019). For the disambiguation to be successful, it is essential that accurate wavelengths are available for the emission lines.

Acknowledgments

The author acknowledges funding from the NASA Heliophysics Data Resource Library, the GSFC Internal Scientist Funding Model competitive work package program, and the

Hinode project. Hinode is a Japanese mission developed and launched by ISAS/JAXA, with NAOJ as domestic partner and NASA and STFC (UK) as international partners. It is operated by these agencies in cooperation with ESA and NSC (Norway).

Facility: Hinode.

ORCID iDs

Peter R. Young https://orcid.org/0000-0001-9034-2925

References

Asplund, M., Amarsi, A. M., & Grevesse, N. 2021, A&A, 653, A141
Behring, W. E., Cohen, L., Feldman, U., & Doschek, G. A. 1976, ApJ, 203, 521
Beintema, D. A., & Pottasch, S. R. 1999, A&A, 347, 942
Cheung, M. C. M., De Pontieu, B., Martínez-Sykora, J., et al. 2019, ApJ, 882, 13
Culhane, J. L., Harra, L. K., James, A. M., et al. 2007, SoPh, 243, 19
Del Zanna, G. 2009, A&A, 508, 501
Del Zanna, G., & Bromage, B. J. I. 1999, JGR, 104, 9753
De Pontieu, B., Martínez-Sykora, J., Testa, P., et al. 2020, ApJ, 888, 3
Dere, K., Del Zanna, G., Young, P., & Landi, E. 2023, ApJS, 268, 52
Edlén, B. 1983, PhyS, 28, 51
Edlén, B. 1985, PhyS, 31, 345
Feuchtgruber, H., Lutz, D., Beintema, D. A., et al. 1997, ApJ, 487, 962
Freeland, S. L., & Handy, B. N. 1998, SoPh, 182, 497
Freeland, S. L., & Handy, B. N., 2012 SolarSoft: Programming and data analysis environment for solar physics, Astrophysics Source Code Library, ascl:1208.013
Handy, B. N., Acton, L. W., Kankelborg, C. C., et al. 1999, SoPh, 187, 229
Harrison, R. A., Sawyer, E. C., Carter, M. K., et al. 1995, SoPh, 162, 233
Kelly, D. M., & Lacy, J. H. 1995, ApJL, 454, L161
Kramida, A., Ryabtsev, A. N., & Young, P. R. 2022, ApJS, 258, 37
Kramida, A. E. 2011, CoPhC, 182, 419
Landi, E., & Young, P. R. 2009, ApJ, 706, 1
Lemen, J. R., Title, A. M., Akin, D. J., et al. 2012, SoPh, 275, 17
Martin, W. C., & Zalubas, R. 1980, JPCRD, 9, 1
Martin, W. C., & Zalubas, R. 1983, JPCRD, 12, 323
Pottasch, S. R., & Beintema, D. A. 1999, A&A, 347, 975
Reconditi, M., & Oliva, E. 1993, A&A, 274, 662
Ryabtsev, A. N., Kononov, E. Y., & Young, P. R. 2022, ApJ, 936, 60
Tripathi, D., Mason, H. E., Dwivedi, B. N., del Zanna, G., & Young, P. R. 2009, ApJ, 694, 1256
Ugarte-Urra, I., & Warren, H. P. 2011, ApJ, 730, 37
Warren, H. P., & Brooks, D. H. 2009, ApJ, 700, 762
Warren, H. P., Ugarte-Urra, I., Young, P. R., & Stenborg, G. 2011, ApJ, 727, 58
Wendeln, C., & Landi, E. 2018, ApJ, 856, 28
Young, P. R. 2022a, EIS Mapper, v1, Zenodo, doi:10.5281/zenodo.6574455
Young, P. R. 2022b, EIS_AUTO_FIT and SPEC_GAUSS_EIS: Gaussian fitting routines for the Hinode/EIS mission, v3.1, Zenodo, doi:10.5281/zenodo.6339584
Young, P. R., Del Zanna, G., Mason, H. E., et al. 2007, PASJ, 59, S727
Young, P. R., Dupree, A. K., Espey, B. R., & Kenyon, S. J. 2006, ApJ, 650, 1091
Young, P. R., & Landi, E. 2009, ApJ, 707, 173
Young, P. R., O'Dwyer, B., & Mason, H. E. 2012, ApJ, 744, 14
Young, P. R., Ryabtsev, A. N., & Landi, E. 2021, ApJ, 908, 104
Young, P. R., & Ugarte-Urra, I. 2022, SoPh, 297, 87
Young, P. R., & Viall, N. M. 2022, ApJ, 938, 27